A multi-term solution of the space-time Boltzmann equation for electrons in gases and liquids

G. J. Boyle,[1] W. J. Tattersall,[1,2] D. G. Cocks,[1] R. P. McEachran,[2] and R. D. White[1]

[1]*College of Science & Engineering, James Cook University, Townsville, QLD 4810, Australia*

[2]*Plasma and Positron Research Laboratories,*
Research School of Physical Sciences and Engineering,
Australian National University, Canberra, ACT 0200, Australia

Abstract

In this study we have developed a full multi-term space-time solution of Boltzmann's equation for electron transport in gases and liquids. A Green's function formalism is used that enables flexible adaptation to various experimental systems. The spatio-temporal evolution of electrons in liquids in the non-hydrodynamic regime is benchmarked for a model Percus-Yevick (PY) liquid against an independent Monte Carlo simulation, and then applied to liquid argon. The temporal evolution of Franck-Hertz oscillations in configuration and energy space are observed for the model liquid with large differences apparent when compared to the dilute gas case, for both the velocity distribution function components and the transport quantities. The packing density in the PY liquid is shown to influence both the magnitude and wavelength of Franck-Hertz oscillations of the steady-state Townsend simulation. Transport properties are calculated from the non-hydrodynamic theory in the long time limit under steady-state Townsend conditions which are benchmarked against hydrodynamic transport coefficients. Finally, the spatio-temporal relaxation of low-energy electrons in liquid argon was investigated, with striking differences evident in the spatio-temporal development of the velocity distribution function components between the uncorrelated gas and true liquid approximations, due largely to the presence of a Ramsauer minimum in the former and not in the latter.

I. INTRODUCTION

The study of electron transport in dense gases and liquids is of interest in understanding the fundamental microscopic scattering processes involved, and to technological applications including liquid-state electronics [1], high-energy particle detectors [2–5], plasma medicine [6–9] and radiation dosimetry [10–13]. For these technologies, the maximisation of their effectiveness requires a detailed understanding of the full spatio-temporal behaviour of electrons in dense gases, liquids, and other bio-structures, typically under non-equilibrium conditions.

In a recent paper [14] the transport of excess electrons in liquid argon was considered from ab initio liquid phase cross-sections calculated using the Dirac-Fock scattering equations. The approach detailed in the seminal works by Lekner and Cohen [15, 16] has been revisited with modern scattering theory techniques, where the original treatment was extended to consider multipole polarizabilities and a non-local treatment of exchange. With an increase in density, several effects become significant, most notably (i) the coherent scattering from multiple scattering centres, (ii) the screening of the long range polarization potential due to induced multipoles in the bulk, and (iii) the contribution of the bulk to the effective potential experienced by the electron. Transport coefficients such as drift velocities and characteristic energies calculated in the hydrodynamic regime with our hydrodynamic multi-term Boltzmann equation solution were in good agreement with swarm experiment measurements in both gas- and liquid-phase argon [14].

In this work we aim to model typical behaviour in Liquid Argon Time Projection Chambers (LArTPC) which are currently being used for high energy particle detection [2], by extending our previous work to an investigation of the liquid state in the non-hydrodynamic regime, using the same electron-argon potentials and cross-sections presented in [14]. In these chambers, ionized electrons originating from the high energy particles are accelerated in the liquid argon under the action of an electric field to generate a current and consequently allow the reconstruction of the path of the high energy particle. Crucial to enhancing detector accuracy is understanding the time-lag between the detector signal t_s and the passage of the high energy particle, t_0. Typically the fluid is chosen such that the drift velocity $W(E)$ is constant over a range of fields (E), and the drift distance during this time is assumed to be $d = \int_{t_0}^{t_\mathrm{s}} W(E)dt$, where effects of diffusion are ignored. In reality however, there is spatial and temporal relaxation of the average velocity of the electrons emanating from the particle

2

track, and hence, to enhance the spatial resolution of these detectors, a full understanding of the spatial and temporal evolution of the phase-space distribution is required.

The solution of the the full temporal-, spatial- and energy-dependent Boltzmann equation is formidable, both mathematically and computationally. Historically, the majority of kinetic theory investigations have focused on the hydrodynamic regime where spatial gradients are small, and have considered increasingly complex space- and time-dependent hydrodynamic behaviours and field configurations (see reviews [17–21]). In situations where the hydrodynamic regime is not applicable, the space-time dependence of the phase space distribution function cannot be projected onto the number density and a density gradient expansion is no longer valid. Instead the configuration-space dependence of the Boltzmann equation must be treated on equal footing with the energy-space dependence, which makes for a difficult problem even for simple geometries [22–24]. It is no surprise that systematic studies of non-hydrodynamic phenomena lag behind their hydrodynamic counterparts. The prototypical example of non-hydrodynamic phenomena is the Franck-Hertz experiment [25, 26], which helped lay the foundations for quantum and atomic physics. Extensive theoretical studies of non-hydrodynamic electron phenomena have been performed including field free spatial relaxation [27], and spatial relaxation in the presence of uniform [28–31], non-uniform [32] and periodic electric fields [33–35]. Similar kinetic studies on the spatial relaxation of electrons in gases in uniform and spatially-varying fields have been performed by Golubovskii et al. [36–39]. White, Robson and co-workers have considered arbitrary electric and magnetic field configurations with a multi-term analysis [18, 40, 41]. Multi-term solutions of the space-dependent Boltzmann equation for semiconductor device simulation have been reviewed by Rupp et al. [42]. Solution of the Boltzmann equation for electrons including both the space and time dependence have also previously been performed [43–45], however these were restricted to a two-term approximation in Legendre polynomials to make the problem computationally feasible. The two-term approximation has also been used to reduce a six-dimensional Boltzmann equation to a four-dimensional Fokker-Planck equation, to model electrons in plasmas, semiconductors and gas discharges [46–48]. Limitations of the two-term approximation for molecular gases are well known [49], however one can estimate from the cross-sections where it may fail [50]. Direct numerical procedures exist that do not require a spherical harmonic expansion to solve the space and time Boltzmann equation [46, 51–56], and there are respective advantages between the two techniques. Although there

are previous works which solve the numerical advection (e.g. the Vlasov equation [57]), these do not include the dominant contribution of the collision term which is present in the full Boltzmann equation.

In this study, we present a full multi-term space-time dependent solution of Boltzmann's equation, capable of handling highly non-equilibrium electron transport in dilute gases, dense gases and liquids under non-hydrodynamic conditions. To our knowledge, this is the first time such a complete solution of Boltzmann's equation has been developed. In addition, by solving for the spatio-temporal evolution of the Boltzmann equation Green's function, the technique is quite general in its application, enabling various experimental configurations (temporal and spatial initial and boundary conditions) and practical devices to be modelled from a single solution. This work extends the Boltzmann equation framework to applications and accuracies comparable to those achieved using the Monte-Carlo simulations of Petrovic, Dujko and co-workers [58–60].

We begin the paper in Section II with a brief overview of the multi-term solution of the full space-time Boltzmann's equation for electrons in structured materials, such as liquids. In Section III we then validate our solution technique against an independent Monte Carlo simulation for a model hard-sphere liquid system with a Percus-Yevick structure factor used to simulate a prototypical liquid with realistic pair correlations. A simple inelastic channel is included to induce oscillatory structures (an idealized version of the well known Franck-Hertz experiment [26]) which can act as a non-hydrodynamic benchmark particularly relevant for noble-gas liquids. The transport properties calculated from the non-hydrodynamic code are compared with those determined from a the previous purely hydrodynamic formalism and associated code [14, 61] in the hydrodynamic limit. Next, in Section IV we investigate the temporal and spatial evolution of the phase-space distribution for electrons in liquid argon, using microscopic cross-sections which have been derived previously [14]. The differences in transport quantities, particularly average velocity, between gaseous systems with increased density and true liquid systems is striking, with implications to applications such as liquid argon time projection chambers. Conclusions are drawn in Section V. A detailed discussion of the numerical code developed and other numerical considerations is given in the Appendix.

4

II. THEORY

The fundamental kinetic equation describing the evolution of an electron swarm in a gaseous or liquid background medium subject to an electric field, $\mathbf{E}$, is the Boltzmann equation for the phase-space distribution function $f \equiv f(\mathbf{r}, \mathbf{v}, t)$ [62]:

$$\left(\frac{\partial}{\partial t} + \mathbf{v} \cdot \frac{\partial}{\partial \mathbf{r}} + \frac{e\mathbf{E}}{m} \cdot \frac{\partial}{\partial \mathbf{v}} \right) f = -J(f), \tag{1}$$

where t is time, and $\mathbf{r}$, $\mathbf{v}$, e and m are the position, velocity, charge and mass of the electron respectively. The collision operator $J(f)$ accounts for interactions between the electrons and the background material, and describes the effect of collisions on the distribution function at a fixed position and velocity. Macroscopic transport properties including mean energy and drift velocity can then be found via expectation values of the distribution, as detailed in Section II B.

The starting point for most modern solutions of the Boltzmann equation is the decomposition of the angular part of the velocity dependence of equation (1) in terms of spherical harmonics [62]. If there is a single preferred direction in the system, e.g. due to an electric field in plane parallel geometry, then the angular dependence of the velocity component can be adequately described by a simpler expansion in terms of Legendre polynomials. For the plane-parallel geometry considered in this work, $f(\mathbf{v}, \mathbf{r}, t)$ can be written as $f(v, z, \mu, t)$, where z is the distance in the direction of the electric field and $\mu = \hat{\mathbf{v}} \cdot \hat{\mathbf{E}}$, such that

$$f(\mathbf{v}, \mathbf{r}, t) = \sum_{l=0}^{\infty} f_l(v, z, t) P_l(\mu), \tag{2}$$

where P_l is the l-th Legendre polynomial. Upon substituting the expansion (2) into equation (1) and equating the coefficients of the Legendre polynomials results in the following system of coupled partial differential equations for the f_l:

$$\frac{\partial f_l}{\partial t} + \sum_{p=\pm 1} \Delta_l^{(p)} \left(\frac{2}{m} \right)^{\frac{1}{2}} \left[U^{\frac{1}{2}} \frac{\partial}{\partial z} + eE \left(U^{\frac{1}{2}} \frac{\partial}{\partial U} + p \frac{(l + \frac{3p+1}{2})}{2} U^{-\frac{1}{2}} \right) \right] f_{l+p} = -J_l(f_l), \tag{3}$$

for $l = 0, 1, 2, \ldots, \infty$, where $U = \frac{1}{2} m v^2$, J_l is the Legendre decomposition of the collision operator, and

$$\Delta_l^{(-1)} = \frac{l}{(2l-1)}; \quad \Delta_l^{(+1)} = \frac{(l+1)}{(2l+3)}. \tag{4}$$

Equation (3) represents an infinite set of coupled partial differential equations for the expansion coefficients, f_l. In practice, one must truncate the series (2) at a sufficiently high index, $l = l_{\max}$. The history of charged particle transport in gases and liquids has been dominated by the 'two-term approximation', i.e., $l_{\max} = 1$. The assumption of quasi-isotropy necessary for the two-term approximation is violated in many situations, particularly when inelastic collisions are included [63] or when higher order moments are probed [14]. Our multi-term formalism avoids these assumptions. Instead, the truncation parameter $l_{\max}$ is treated as a free parameter that is incremented until some convergence criterion is met on the distribution function or its velocity moments.

In order to solve equation (3) we require the collision operators for all of the relevant collisional processes, and their representations in terms of Legendre polynomials, J_l. If we assume that the neutral background material is at rest and in thermal equilibrium at a temperature T_0, then the collision operator is linear in the swarm approximation. Below we detail the specific forms of the collision operator for the particle-conserving elastic and inelastic collisions employed. A further expansion of each collision integral with respect to the ratio of swarm particle mass to neutral particle mass, m/m_0, has been performed. Because this ratio is small for electrons in fluids, only the leading term of this expansion was taken into account in each equation of the system (3). In our case the total collision operator separates into $J_l = J_l^{\mathrm{el}} + J_l^{\mathrm{exc}}$ where J_l^{el} and J_l^{exc} are the elastic and inelastic collision operators, respectively. For dense mediums and low electron energies, the de Broglie wavelength of the electron is comparable to the average inter-particle spacing $\sim n_0^{-1/3}$ where n_0 is the background medium number density, implying that the electron wave is scattered coherently from multiple scattering centres in the medium. Cohen and Lekner [16] showed how to account for coherent scattering using a two-term approximation, which has since been extended to a multi-term regime [62, 64]. The Legendre projections of the elastic collision operator in the small mass ratio limit were shown to be:

$$J_l^{\mathrm{el}}(f_l) = \begin{cases} -\frac{2m}{m_0} U^{-\frac{1}{2}} \frac{\partial}{\partial U} \left[U^{\frac{3}{2}} \nu_1^{\mathrm{el}}(U) \left(f_0 + k_{\mathrm{b}} T_0 \frac{\partial f_0}{\partial U} \right) \right] & l = 0, \\ \tilde{\nu}_l^{\mathrm{el}}(U) f_l(U) & l \geq 1. \end{cases} \quad (5)$$

Here, m_0 is the mass of the background neutral, k_{b} is Boltzmann's constant, and

$$\nu_l^{\mathrm{el}}(U) = n_0 \left(\frac{2U}{m} \right)^{\frac{1}{2}} \left(2\pi \int_0^\pi \sigma(U, \chi) \left[1 - P_l(\cos \chi) \right] \sin \chi \, d\chi \right), \quad (6)$$

are the usual binary collision frequencies where $\sigma(U, \chi)$ is the atomic cross section, modified for polarisation screeening [14]. The $\tilde{\nu}_l^{\mathrm{el}}(v)$ in equation (5) are the structure-modified counterparts to $\nu_l^{\mathrm{el}}(U)$, i.e.,

$$\tilde{\nu}_l^{\mathrm{el}}(U) = n_0 \left(\frac{2U}{m}\right)^{\frac{1}{2}} \left(2\pi \int_0^\pi \Sigma(U, \chi)\left[1 - P_l(\cos\chi)\right]\sin\chi d\chi\right), \tag{7}$$

where $\Sigma(U, \chi)$ is the effective structure-modified differential cross-section

$$\Sigma(U, \chi) = \sigma(U, \chi)\, S\left(\frac{2}{\hbar}\sqrt{2mU}\sin\frac{\chi}{2}\right), \tag{8}$$

which accounts for coherent scattering effects through the static structure factor, $S\left(\frac{2}{\hbar}\sqrt{2mU}\sin\frac{\chi}{2}\right)$ [16]. At higher energies, the de Broglie wavelength becomes much less than the inter-particle spacing and the effects of coherent scattering are no longer important. In this limit, the binary scattering approximation is recovered, i.e., $\Sigma \to \sigma$ and $\tilde{\nu}_l^{\mathrm{el}} \to \nu_l^{\mathrm{el}}$. ν_1^{el} is more commonly known as the momentum transfer collision frequency, ν_{m}, which is associated with the momentum transfer cross section, σ_{m}. Similarly, $\tilde{\nu}_{\mathrm{m}} = \Sigma_{\mathrm{m}}$ is known as the effective (structure-modified) momentum transfer collision frequency. We will adopt this convention in the following discussions.

At higher fields, incoherent inelastic scattering effects, such as electronic excitations, need to be included [62, 64]. By considering only a single inelastic channel, and assuming neutral particles are in the ground state, the excitation collision operator is

$$J_l^{\mathrm{exc}}(f_l) = \nu^{\mathrm{exc}}(U)\,f_l(U) - \begin{cases} \left(\frac{U+U_{\mathrm{I}}}{U}\right)^{\frac{1}{2}}\nu^{\mathrm{exc}}(U+U_{\mathrm{I}})\,f_l(U+U_{\mathrm{I}}), & l = 0, \\[2mm] 0, & l \geq 1, \end{cases} \tag{9}$$

where U_{I} is the threshold energy associated with the excitation collision frequency ν^{exc}.

Now that the form of the collision operators are known, the kinetic equation (3) can be solved numerically. The numerical approach employed in this work can be summarized as a simplified flux corrected transport method [65] for the configuration-space sub problem, a centered difference discretization in energy and implicit Euler method in time [61] for the energy-space sub problem, combined via Lie-Trotter splitting [66, 67]. A detailed discussion of the numerical techniques employed in this work is given in the appendix.

A. Green's function solution

In our formalism and associated non-hydrodynamic code, we solve for the Green's function of the Boltzmann equation,

$$\mathcal{L}\tilde{f}_l = \delta(z - z_0)\delta(t - t_0), \tag{10}$$

where

$$\mathcal{L}f_l = \frac{\partial f_l}{\partial t} + \left(\frac{2}{m}\right)^{\frac{1}{2}} \sum_{p=\pm 1} \Delta_l^{(p)} \left[U^{\frac{1}{2}}\frac{\partial}{\partial z} + \frac{eE}{m}\left(U^{\frac{1}{2}}\frac{\partial}{\partial U} + p\frac{\left(l + \frac{3p+1}{2}\right)}{2}U^{-\frac{1}{2}}\right)\right] f_{l+p} + J_l\left(f_l\right) \tag{11}$$

for $l = 0, 1, 2, \ldots, \infty$. The Green's function solution, f_l, can then be used to find the solution of the more general space-time Boltzmann equation, i.e. if

$$\mathcal{L}f_l = S(z, t), \tag{12}$$

where $S(z, t)$ is a source term, then

$$f_l\left(U, z, t\right) = \int dt_0 \int dz_0 \, \tilde{f}_l\left(U, z - z_0, t - t_0\right) S\left(z_0, t_0\right). \tag{13}$$

We do this by choosing an initial distribution in configuration-space that is a good approximation to a delta-function, which, for this study, is a narrow Gaussian,

$$\delta_a(z) = \frac{1}{a\sqrt{\pi}} \exp\left(-\frac{z^2}{a^2}\right), \tag{14}$$

where a is a parameter controlling the width of the Gaussian, representing the temporal-spatial relaxation profile of a single pulse centred on z_0 and released at t_0. In the limit of $a \to 0$, $\delta_a(z) \to \delta(z)$. The formalism is quite general, enabling the treatment of various experiments (e.g. Pulsed Townsend (PT), Steady-State Townsend (SST) and other drift tube configurations [68]), as well as various source and spatial/energy/temporal distributions, through a single solution. This approach extends the functionality and accuracy of Boltzmann equation solutions to those routinely achieved by Monte Carlo simulations [58, 69, 70].

B. Transport properties

The transport properties that represent experimental measurables are obtained as averages of certain quantities with respect to the distribution function, f. Among the transport

properties of interest in the current manuscript are the number density, n, particle flux, Γ, and average energy, ϵ, of the electron swarm, which are calculated via

$$n\left(z,t\right) = 2\pi \left(\frac{2}{m}\right)^{\frac{3}{2}} \int dU \; U^{\frac{1}{2}} f_0(U,z,t), \tag{15}$$

$$\Gamma\left(z,t\right) = \frac{2\pi}{3} \left(\frac{2}{m}\right)^{2} \int dU \; U f_1(U,z,t), \tag{16}$$

$$\epsilon\left(z,t\right) = \frac{1}{n\left(z,t\right)} 2\pi \left(\frac{2}{m}\right)^{\frac{3}{2}} \int dU \; U^{\frac{3}{2}} f_0(U,z,t). \tag{17}$$

Likewise, we sample the traditional hydrodynamic transport coefficients in this non-hydrodynamic framework, i.e. the drift velocity, W, and the (longitudinal) diffusion coefficient, D_{L}:

$$W(t) = \frac{d}{dt}\left[\frac{1}{N\left(t\right)}\left(\int dz \; z n\left(z,t\right)\right)\right], \tag{18}$$

$$D_{\mathrm{L}}(t) = \frac{1}{2}\frac{d}{dt}\left[\frac{1}{N\left(t\right)}\left(\int dz \; z^2 n\left(z,t\right)\right) - \left(\frac{1}{N\left(t\right)}\int dz \; z n\left(z,t\right)\right)^2\right], \tag{19}$$

where $N(t)$ is

$$N\left(t\right) = \int dz \; n\left(z,t\right). \tag{20}$$

As we work with a plane-parallel geometry, $N(t)$ in equation (20) actually represents the contribution to density in the directions perpendicular to the field, which we scale out. To be explicit, the normalization of $n(\boldsymbol{r},t) = n(z,t)$ is chosen according to equation (20).

In this work we are interested in the results of a SST simulation, for which there have been previous calculations performed for benchmark systems. Similar to [58], the SST transport properties can be determined from the Green's function transport properties via

$$f_l^{\mathrm{SST}}\left(U,z\right) = h \int_0^\infty dt_0 \; \tilde{f}_l\left(U,z,t_0\right), \tag{21}$$

$$n_{\mathrm{SST}}(z) = h \int_0^\infty dt_0 \; \tilde{n}\left(z,t_0\right), \tag{22}$$

$$\Gamma_{\mathrm{SST}}\left(z\right) = h \int_0^\infty dt_0 \; \tilde{\Gamma}\left(z,t_0\right), \tag{23}$$

$$\epsilon_{\mathrm{SST}}\left(z\right) = \frac{h}{n_{\mathrm{SST}}(z)} \int_0^\infty dt_0 \; \tilde{n}\left(z,t_0\right)\tilde{\epsilon}\left(z,t_0\right), \tag{24}$$

9

where h is the emission rate of the source and the tilde quantities refer to equations (15)–(17) with the Green's function $\tilde{f}_l$. In practice the upper limit of the integrals is not ∞, but a sufficiently long time for the SST transport properties to have converged over the range of z considered.

C. Reduced variables

Henceforth, it is convenient to work with rescaled reduced variables.In particular, the space and time variations will be presented as functions of

$$z^* = n_0 \sigma_0 z, \tag{25}$$

$$t^* = n_0 \sigma_0 \sqrt{\frac{2e}{m}} t, \tag{26}$$

$$n^* = \frac{n}{n_0 \sigma_0 N} \tag{27}$$

where $\sigma_0 = 10^{-20}$ m^2 and N is defined in equation (20). Likewise, the electric field dependence arises through the reduced electric field E/n_0 in units of Townsend (1 Td $= 10^{-21}$Vm^2). By presenting results in this manner the n_0 dependence is scaled out, which allows for comparisons between the dilute gas phase and the liquid/dense gas phase, to give a true reflection of the impact of coherent and other scattering effects.

III. VALIDATION OF ELECTRON TRANSPORT USING A BENCHMARK LIQUID MODEL

In this section we validate our theory and numerical code against a model system that includes structure effects. A benchmark frequently employed in the literature which treats a structured system is that for a system of hard-sphere potentials obtained by applying the Percus-Yevick approximation as a closure to the Ornstein-Zernike equation, which yields a pair-correlation function [71, 72] and corresponding static structure factor. We include the corrections of Verlet-Weiss [73, 74] which better emulate the structure of a real liquid (see [70] for details). The volume fraction parameter, Φ, specifies how tightly packed the hard spheres in the medium are. It can be written in terms of the hard-sphere radius r and the neutral number density, n_0, as $\Phi = \frac{4}{3}\pi r^3 n_0$. We have modeled systems with a range of

10

densities, from $\Phi \approx 0$, which approximates a dilute gas, to $\Phi = 0.4$, which states that 40% of the volume is excluded by hard-sphere potentials of the neutral molecules.

The remaining details required of the benchmark hard-sphere model implemented for electron sized particles are

$$
\begin{aligned}
\sigma_{\mathrm{m}} &= 6 \text{ \AA}^2, \\
\sigma^{\mathrm{exc}} &= \begin{cases} 0, & U < 2 \text{ eV} \\ 0.1 \text{ \AA}^2, & U \geq 2 \text{ eV} \end{cases} \\
\Phi &= 0,\ 0.2,\ 0.3,\ 0.4, \\
E/n_0 &= 3 \text{ Td}, \\
m_0 &= 4 \text{ amu}, \\
T_0 &= 0 \text{ K}.
\end{aligned}
\tag{28}
$$

A step-like inelastic process has been included in addition to the standard Percus-Yevick hard sphere benchmark system in model (28). The inelastic channel introduces a periodic oscillatory non-hydrodynamic behaviour, similar to those observed in the well-known Franck-Hertz experiment, and can hence determine whether the numerical code is accurately capturing the non-hydrodynamic phenomena. Figure 1 highlights the variation of the effective momentum transfer cross-section with Φ, evaluated using the cross-section in (28) together with the static structure factor from [70]. At high energies, coherent scattering effects are suppressed, and the various momentum transfer cross sections converge on the dilute gas case (corresponding to $\Phi = 0$) .
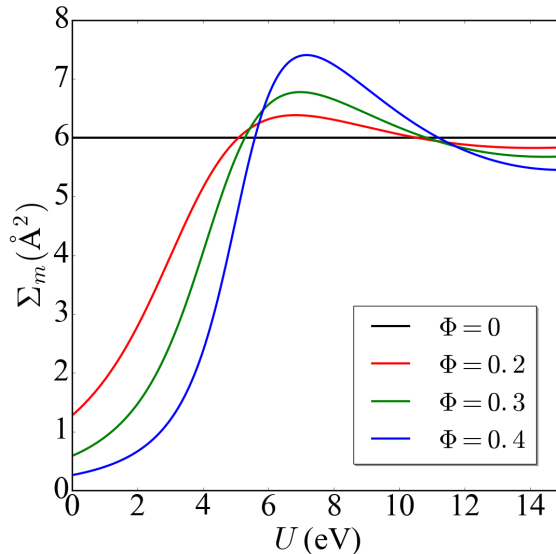
Figure 1: The variation of the effective elastic momentum-transfer cross-section, $\Sigma_{\mathrm{m}} = 2\pi \int_0^\pi \Sigma(U,\chi)\left[1 - \cos\chi\right]\sin\chi d\chi$, including structure with energy for model (28) for various volume fractions, Φ.

The source distribution is given by

$$f\left(\mathbf{v}, \mathbf{r}, 0\right) = N f_{\mathrm{DM}}(\mathbf{v}) f_z(z), \tag{29}$$

where $f_{\mathrm{DM}}(\mathbf{v})$ is a drifted Maxwellian distribution with $T = 10^4$ K and $\mathbf{W} = 10^5$ ms$^{-1}\hat{\mathbf{E}}$, i.e.,

$$f_{\mathrm{DM}}(\mathbf{v}) = \left(\frac{m}{2\pi k_{\mathrm{b}} T}\right)^{\frac{3}{2}} \exp\left[-\frac{m}{2k_{\mathrm{b}} T}\left(\mathbf{v} - \mathbf{W}\right)^2\right], \tag{30}$$

while $f_z(z)$ is a narrow Gaussian in configuration-space, i.e.,

$$f_z(z) = \frac{1}{\Delta z_0 \sqrt{2\pi}} \exp\left(-\frac{1}{2}\left(\frac{z}{\Delta z_0}\right)^2\right). \tag{31}$$

For the benchmark model we take $\Delta z_0 = 0.1$. Note that, by the choice of normalization in equations (31)–(30), we have $2\pi \left(\frac{2}{m}\right)^{\frac{3}{2}} \iint U^{\frac{1}{2}} f_0(U,z,0) \, dU dz = N$.

A. Transport coefficients in the long-time hydrodynamic limit

In previous papers [14, 61] a purely hydrodynamic formalism and associated numerical code has been developed for light particles in gases and liquids. We compare with the

12

asymptotic values of the drift velocity and diffusion coefficient calculated from the spatial moments (18) and (19) respectively and show these in Table I. We also show the differences between two-term and multi-term calculations which can be up to 2.3%, for the model (28).

The zeroth order hydrodynamic transport coefficients, i.e., the mean energy and drift velocity, agree to within 0.2% with the multi-term asymptotic non-hydrodynamic values for the volume fractions considered. The multi-term hydrodynamic and non-hydrodynamic calculations of the longitudinal diffusion coefficient agree to within 0.7%. As the volume fraction increases, all of the coefficients increase monotonically, a consequence of the coherent scattering. At low energies, increasing volume fractions leads to decreased momentum-transfer cross-sections. For further discussion on the physical variation of the hydrodynamic transport coefficients with volume fraction the reader is referred to [62, 70, 75]. The close agreement between the asymptotic non-hydrodynamic and multi-term hydrodynamic transport properties serves to validate the long-time behaviour of our space-time solution to Boltzmann's equation.

Table I: Comparison of the steady-state transport quantities calculated from multi-term non-hydrodynamic (MTN), multi-term hydrodynamic (MT) and two-term hydrodynamic (2T) formalism for model (28) at various volume fractions Φ.

Φ	Method	ϵ	W	$n_0 D_{\mathrm{L}}$
		[eV]	$[10^4\,\mathrm{ms}^{-1}]$	$[10^{24}\,\mathrm{m}^{-1}\mathrm{s}^{-1}]$
0	MTN	0.8335	1.385	2.386
	MT	0.8337	1.385	2.387
	2T	0.8337	1.386	2.383
0.2	MTN	0.9765	3.397	6.333
	MT	0.9772	3.391	6.328
	2T	0.9788	3.402	6.307
0.3	MTN	1.080	5.929	11.22
	MT	1.080	5.921	11.24
	2T	1.086	5.970	11.16
0.4	MTN	1.233	10.52	19.51
	MT	1.233	10.51	19.63
	2T	1.255	10.75	19.33

B. Space-time evolution of the phase-space distribution and its velocity moments

We now consider the effect of the volume fraction in model (28) on the spatio-temporal evolution of the phase-space distribution and hence the transport properties. In Figure 2 the evolution of the f_0 and f_1 velocity distribution function components are compared for $\Phi = 0$ and $\Phi = 0.4$ at three different times, and the integral moments of f_0, the electron density n^*, and velocity moment of f_1, the flux Γ^*, are displayed in Figure 3. The time scale for variation of f_0 is governed by $\sim \left(2\frac{m}{m_0}\nu_{\mathrm{m}}\right)^{-1}$, and hence exhibits no explicit Φ dependence in the time scale, however differences arise due to the implicit energy dependence in the collision frequency and the coupling to higher order moments with different time scales. The time scale for variation of f_1 on the other hand is governed by $\tilde{\nu}_{\mathrm{m}}^{-1}$, which has an explicit Φ dependence. The time scale for momentum exchange is significantly decreased for

increasing Φ at low energies, as shown in Figure 1, however they approach the same value at higher energies.

At very small times (e.g. $t^* = 0.2$), there are only small differences in the f_0 contours between the two volume fractions, and this is also highlighted in the density n^*. At higher energies (> 5-6 eV) there are also very little differences in the f_1 contours (reflecting the similarity in the momentum relaxation times at these energies), however at low energies, the $\Phi = 0.4$ contours for f_1 are significantly displaced in both energy and configuration-space relative to the $\Phi = 0$ case. This indicates significantly higher advective and diffusive fluxes in this energy regime, which is evidenced in the flux profiles of Figure 3.

At larger times, the f_0 and f_1 contours in the $\Phi = 0.4$ case depart significantly from the $\Phi = 0$ case, initially in the low energy regime and then finally the entire energy regime as the higher energy electrons relax from the initial condition. The peaks in each of the distribution components at larger times for $\Phi = 0.4$ case are displaced significantly more in the z-direction. This is reflected in both the density and flux profiles at larger times, which highlight the enhanced drift and diffusion due to the reduced momentum transfer cross-section associated with coherent scattering for this model and field. Interestingly, at sufficiently long times, the $\Phi = 0.4$ contours have predominantly positive values, and only very small negative excursions at low energies, in contrast to the $\Phi = 0$ contours. At these times, the flux is positive over the swarm indicating that the advective contribution dominates the diffusion contribution, since the density gradients are much more rapidly dissipated in the $\Phi = 0.4$ case.

Strikingly, both the $\Phi = 0$ and $\Phi = 0.4$ contours for both f_0 and f_1 demonstrate periodic structures in both configuration space and in energy space at sufficiently long times and sufficiently downstream from the source. The periodic structures manifest themselves earlier for the $\Phi = 0.4$ case. These are the well known Franck-Hertz oscillations [25, 26]. A simplistic picture of this non-hydrodynamic phenomena is that the electrons in the swarm are being repeatedly accelerated by the electric field to an energy above the inelastic process threshold whereby they undergo an inelastic collision losing their energy. This simple physics is evidenced in the f_0 and f_1 distributions. By integrating over the energy to obtain the density and flux, shown in Figure 3, much of the periodic structure observed in the distribution function is masked, however some non-Gaussian spatial structure is still observed. We will explore the Φ-dependence of the wavelengths of oscillations further in Section III C.
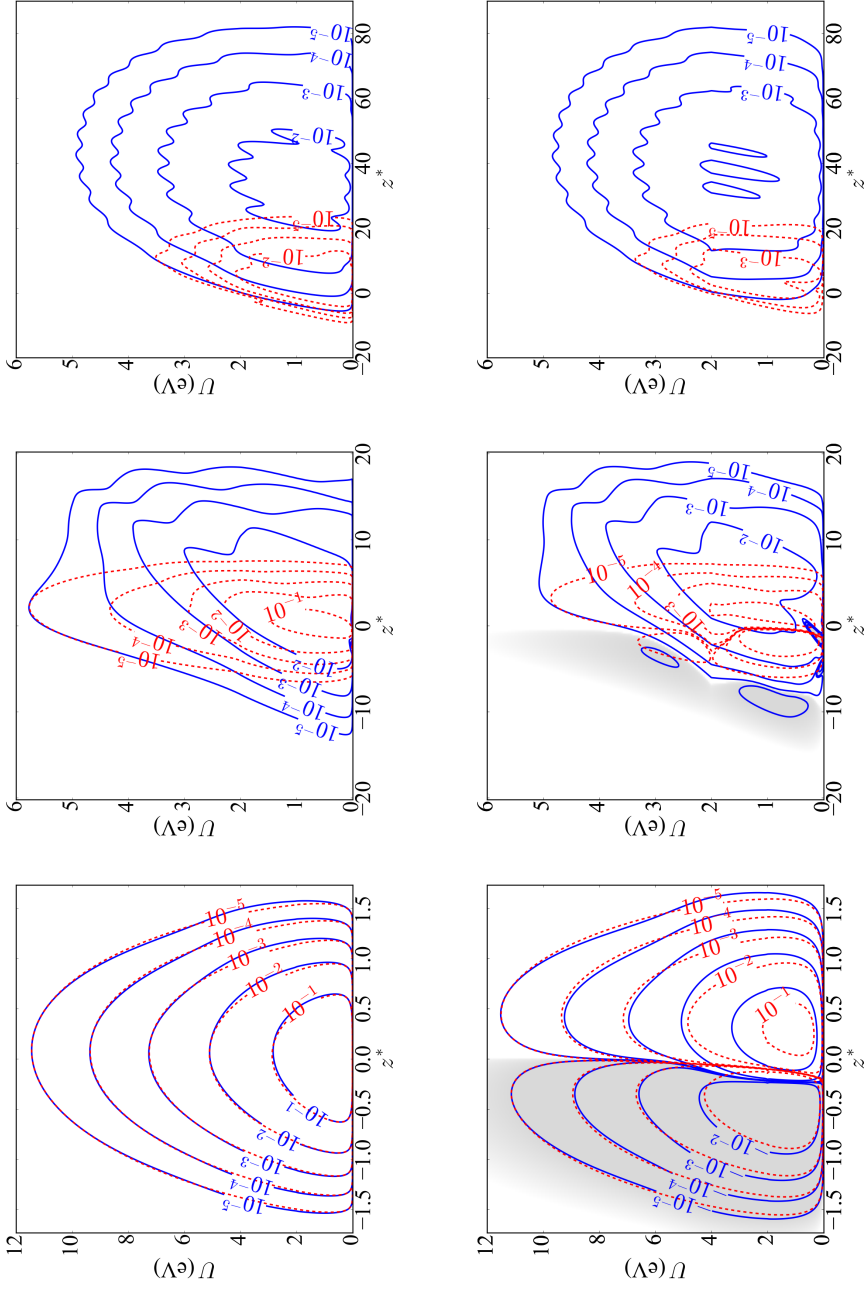
Figure 2: Temporal evolution of the distribution function components for model (28) with $\Phi = 0$ (dashed lines) and $\Phi = 0.4$ (solid lines). The first row are $2\pi\sigma_0 \left(\frac{2}{m}\right)^{\frac{3}{2}} U^{\frac{1}{2}} f_0/n_0$ (eV^{-1}) contours while the second row are $\left|2\pi\sigma_0 \left(\frac{2}{m}\right)^{\frac{3}{2}} U f_1/n_0\right|$ (eV$^{-\frac{1}{2}}$) contours. The three columns represent the times, $t^* = 0.2$, 20, and 200 respectively. The shaded contours indicate $U f_1 < 0$.
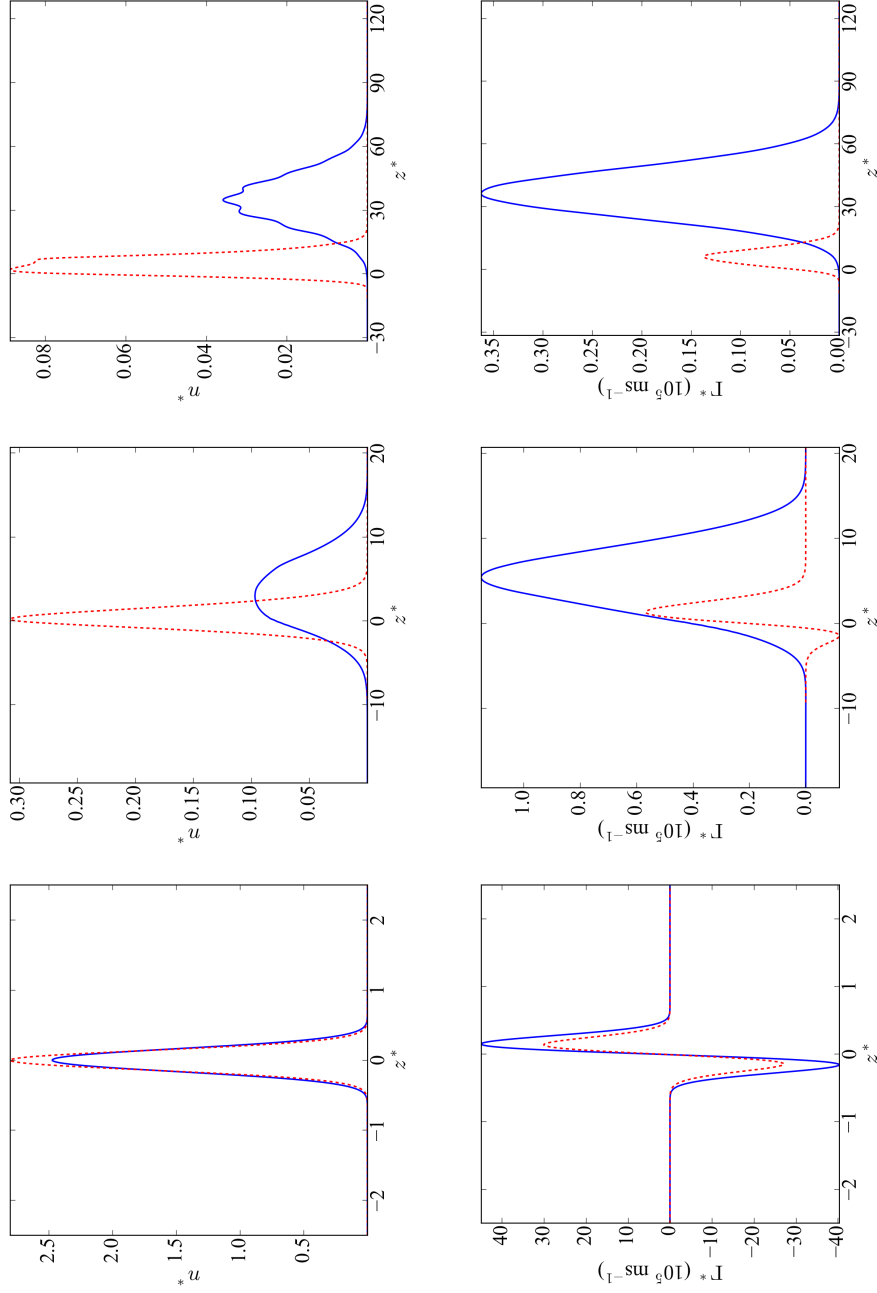
16

Figure 3: Temporal evolution of the spatially varying density n^* and flux $\Gamma^* = \frac{1}{n_0\sigma_0 N}\Gamma$ for model (28) with $\Phi = 0$ (dashed lines) and $\Phi = 0.4$ (solid lines). The three columns represent the times, $t^* = 0.2$, 20, and 200 respectively.

17

C. Steady-state Townsend configuration

The solution detailed in Section III B is essentially equivalent to solving for the Boltzmann equation Green's function for the model (28). A strict validation of this approach and associated numerical code is to be able to reproduce the Steady-State Townsend (SST) transport properties from the Green's function solution, as described in Section II A. The average energy (24) and average velocity (23) for SST simulations of various volume fractions are shown in Figure 4, along with the results of an independent Monte Carlo simulation (the details of which can be found in [70]). In the spatially asymptotic regime (not shown in Figure 4), the average energy and the average velocity are equal to the hydrodynamic and pulsed-Townsend values shown in Table I. Li and co-workers have investigated the relaxation characteristics of model 28 for $\Phi = 0$ and determined that the steady-state is reached at a distance of $z^* \approx 100$ [40, 76]. It can be seen that the SST properties demonstrate damped spatially periodic structures similar to those observed in the Franck-Hertz experiment and other investigations [25, 26, 30, 77–79]. They are a manifestation of the energy and spatially periodic structures in the distribution function components, and in the spatially periodic structures in the density and flux profiles of Figure 3. By assuming the elastic scattering is weak, the width between the peaks in the transport property profiles, λ, is directly related to the threshold energy of the inelastic process, U_I in eV, via [80]

$$\lambda = \frac{U_I}{(0.1)_{\text{eV/Td}} (E/n_0)_{\text{Td}}}, \tag{32}$$

where the reduced electric field is in Townsend (Td). For model (28), the theoretical spacing is $6.\dot{6}z^*$. In Figure 4 it is possible to see that there are variations in the wavelength of the spatial structures with Φ, as well as significant differences in the decay rates of the oscillation amplitudes. For $\Phi = 0$, the wavelength is approximately 8.00 ± 0.2 and this decreases to 6.67 ± 0.2 for $\Phi = 0.4$. The differences arise explicitly due the differences in the elastic momentum transfer cross-section, as well as implicit variations associated with the modification to the swarm's energy with Φ. Because the effective momentum transfer for larger Φ, the oscillations are not as strongly dampened. This has the effect of making λ for the $\Phi = 0.4$ case closest to the analytical approximation (32), since the reduced momentum transfer more closely approximates the weak elastic scattering assumption used in deriving it. Note that we have compared the SST transport properties calculated using a two-term

approximation (not shown) to the multi-term approximation, which were found to differ by as much as 3% over the range of z^*.

We must also point out that the validity of these profiles are dependent on the discretization of the distributions in configuration-space. If the spatial discretization is of the same order as the Franck-Hertz wavelength, then it will be very difficult to resolve these features in the distributions and consequently the time-averaged profiles. As we use an adaptive mesh that increases the spatial grid spacing with time (see Appendix A 4), we can only accurately resolve the distribution up to a maximum $z^* \approx 30$.
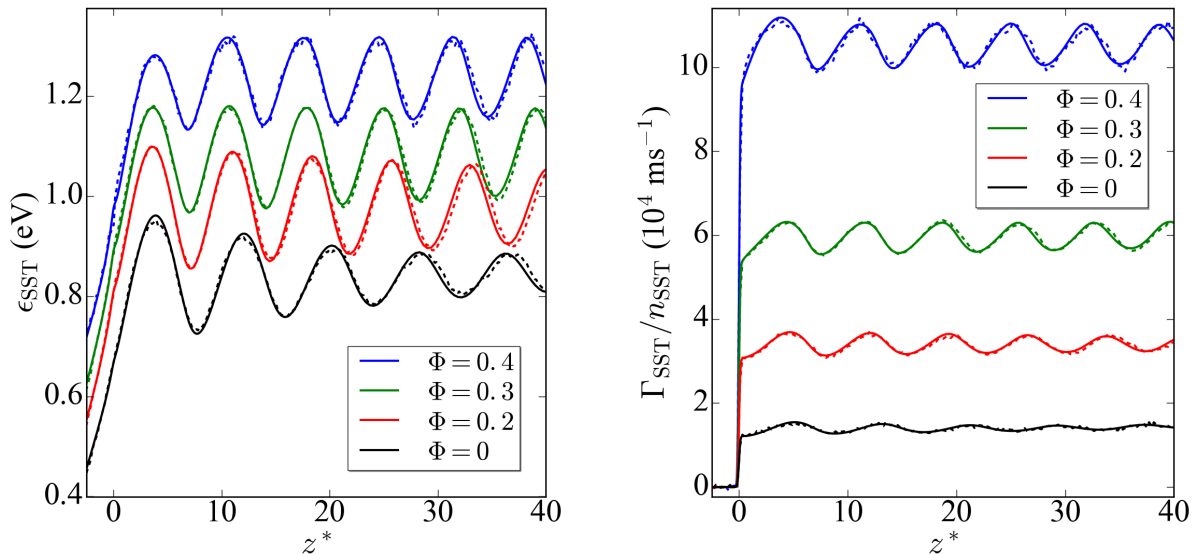

Figure 4: Spatial variation of the average energy and average velocity under SST conditions for model (28) with various volume fractions Φ. The solid lines are solutions of the Boltzmann equation, while the dashed lines are the results of Monte Carlo simulation. The details of the Monte Carlo simulation can be found in [70].

IV. SPATIO-TEMPORAL RELAXATION OF ELECTRONS IN LIQUID ARGON

As detailed in the introduction, to enhance the spatial resolution of Liquid Argon Time Projection Chambers (LArTPC) detectors requires an enhanced understanding of the spatio-temporal evolution typical of ionized electrons emanating from the high energy particle track. Typically these chambers operate with electric field strengths of less than 500 kV/cm. Foxe et al. [81] have measured the energy distribution of the electrons ionized by high

energy particles in liquid argon, and have shown that the majority of the ionized electrons have energies below 1 eV. Consequently in this study we employ an initial source energy-distribution that is constant in energy space up to 1 eV, i.e.,

$$f_U(U) = CU^{-\frac{1}{2}}\Theta\left(U - 1\,\text{eV}\right), \tag{33}$$

where Θ is the Heaviside step function, and U is in eV and C is a normalisation constant. The mean energy of this distribution is 0.5 eV. The swarm is released from a narrow Gaussian in configuration-space,

$$f_z(z) = \frac{1}{\Delta z_0\sqrt{2\pi}}\exp\left(-\frac{1}{2}\left(\frac{z}{\Delta z_0}\right)^2\right), \tag{34}$$

so that the full initial phase-space distribution is $f(\boldsymbol{v},\boldsymbol{r},0) = Nf_U(U)f_z(z)$, and where C is chosen such that $2\pi\left(\frac{2}{m}\right)^{\frac{3}{2}}\iint U^{\frac{1}{2}}f_0(U,z,0)\,dU dz = N$. For argon, we take $\Delta z_0 = \sqrt{10}$, a larger initial spread than for the Percus-Yevick model, reflecting the smaller cross sections of argon, and hence a larger mean free path.

A. Cross-sections, potentials and screening

The procedure for including a real physical cross section differs slightly from the benchmark described in the previous section. As shown in [14], polarisation screening and the effect of the surrounding atoms must be accounted for to obtain an effective cross section $\sigma(U,\chi)$ that is used in equations (6) and (8). The momentum transfer cross-sections calculated from the dilute gaseous and liquid argon potentials are shown in Figure 5. It is significant to note the absence of the Ramsauer minimum in the liquid-phase cross-section. Shown in [14], the gas-phase cross-sections produce transport coefficients that agree with experiment to within 10%. The liquid modifications to these is largely insensitive to the fine detail of the cross section and so retains the same level of accuracy within the approximations used.
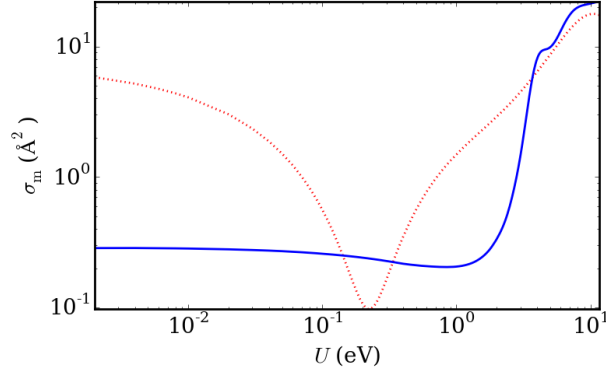
Figure 5: The momentum transfer cross-sections in the gas-phase (dashed line) and liquid-phase (solid line) for electrons in argon [14].

B. Results

In order to consider conditions representative of those in liquid state particle detectors, we simulate electron transport in liquid argon under the following conditions:

$$
\begin{aligned}
E/n_0 &= 2.5 \times 10^{-3} \text{ Td}, \\
T &= 85 \text{ K}, \\
m_0 &= 40 \text{ amu}.
\end{aligned}
\tag{35}
$$

The reduced field is equivalent to 500 kV/cm with a density corresponding to liquid argon, $n_0 = 0.0213 \text{ Å}^{-3}$. For this reduced electric field and source distribution, given in (33)-(34), the electron swarm energies are generally well below the first inelastic channel threshold energy (8.9 eV), so that there is no inelastic channel operative, and hence the periodic spatial structures observed in the Percus-Yevick hard-sphere liquid model above are not present.

The relaxation of the f_0 distribution function component is compared for the gas and liquid phases at three different times in Figure 6. At $t^* = 1$, there are only small differences between the contours reflecting similar energy relaxation rates between the two phases initially. At $t^* = 10$, a bulge is beginning to develop in the gas-phase contour in the energy region between $0.1 - 0.5$ eV, which corresponds to the Ramsauer minimum in the gas-phase momentum transfer cross-section. In this region, the gas-phase momentum transfer cross-section dips below the liquid cross-section, which has resulted in this enhancement of the

21

diffusive flux in this range. At higher energies the liquid cross-section is less than the gas-phase cross-section, which has resulted in enhanced diffusive flux. At $t^* = 100$ these effects are even more pronounced.

In Figure 6 the f_1 component contours for the gas and liquid phases of argon are compared for the same three times. At the first time, $t^* = 1$, there are already significant differences in the f_1 contours, with the largest change occurring in the Ramsauer minimum range in the gas-phase case. This highlights again the difference in the time scales of the energy and momentum relaxation between the two phases. As time increases, greater differences develop between the f_1 contours particularly around the Ramsauer minimum and at the high energy range for the reasons previously discussed.

The number density as a function of time is shown in Figure 7. The behaviour of the number density profiles is consistent with the behaviour of the f_0 and f_1 profiles. At $t^* = 1$ there is no noticeable difference in the two number density profiles. At later times it is clear that, despite the Ramsauer minimum in the gas-phase, the liquid-phase experiences the greater diffusion rate overall. For the electric field considered and initial source distribution, the average drift velocity for both the gas and liquid phases is small compared to the diffusion rates.
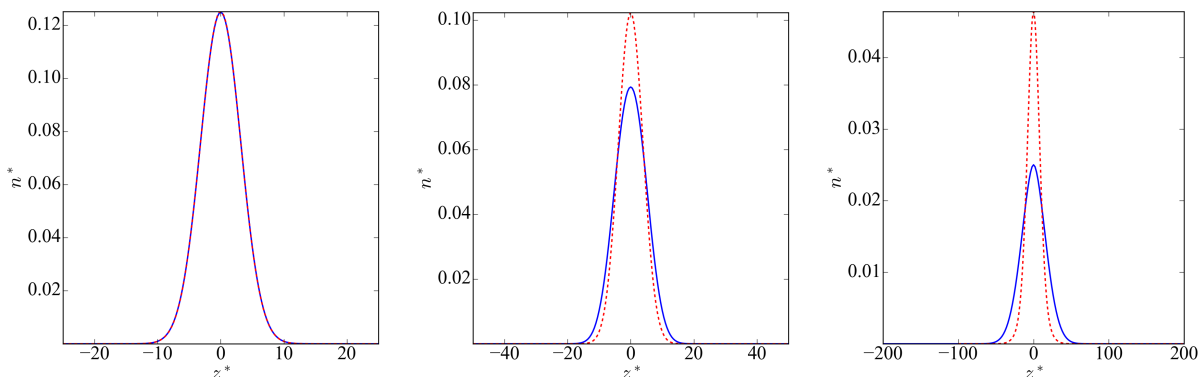

Figure 7: Temporal evolution of the number density profiles n^* for gas-phase (dashed lines) and liquid-phase (solid lines) argon. The three columns represent the times, $t^* = 1$, 10, and 100 respectively.
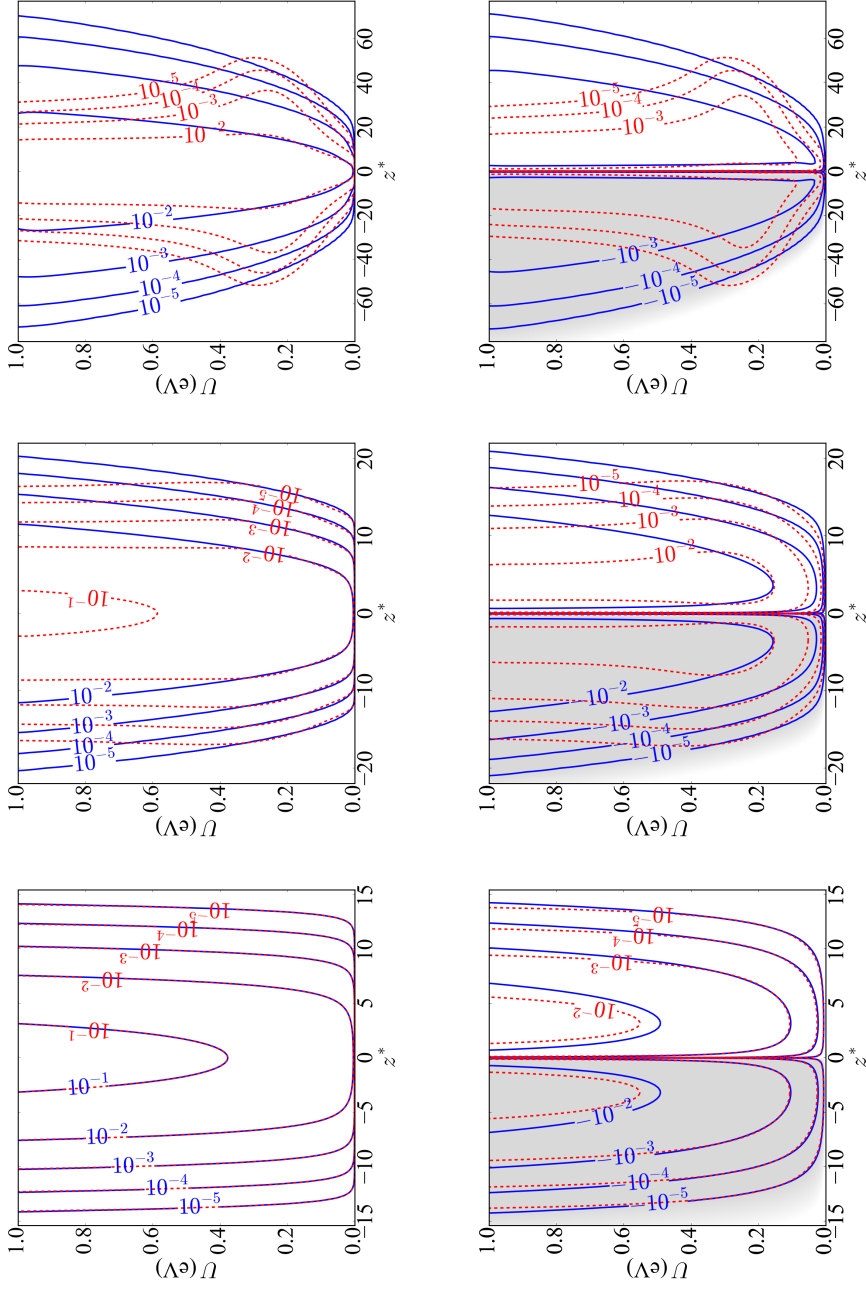
22

Figure 6: Temporal evolution of the distribution function components for gas-phase (dashed lines) and liquid-phase (solid lines) argon. The first row are $2\pi\sigma_0 \left(\frac{2}{m}\right)^{\frac{3}{2}} U^{\frac{1}{2}} f_0/n_0 (\text{eV}^{-1})$ contours, the second row are $\left|2\pi\sigma_0 \left(\frac{2}{m}\right)^{\frac{3}{2}} U f_1/n_0\right| (\text{eV}^{-\frac{1}{2}})$ contours. The shaded contours indicate $U f_1 < 0$. The three columns represent the times, $t^* = 1$, 10, and 100 respectively.

V. CONCLUSIONS

We have developed a full multi-term, space-time dependent solution of the electron Boltzmann equation in gases and liquids capable of modeling non-hydrodynamic conditions. The flexibility of the algorithm lies in solving the Boltzmann equation's Green's function, knowledge of which allows one to construct the solution for other experimental configurations e.g. the SST experiment and similar applications. A tailored numerical scheme has been employed to efficiently evolve the energy-space and configuration-space components.

The theory and associated code was first applied to a simple hard-sphere benchmark model liquid, where structure effects were simulated by the Percus-Yevick structure factor as a function of the volume fraction, Φ. This benchmark emulates Franck-Hertz-type experiments in liquid neon or liquid xenon, and the inclusion of an inelastic channel was a key test of the algorithm's ability to reproduce non-hydrodynamic phenomena. Periodic spatial structures developed in the space-time and steady-state profiles for the distribution function components and associated transport properties, the periodicity of which is directly related to the threshold energy of the inelastic process. We observed that these periodic structures arose on shorter times scales when coherent scattering effects became important. The steady-state profiles constructed for various volume fractions also reproduced the non-hydrodynamic oscillatory structures expected. The asymptotic transport coefficients calculated from the non-hydrodynamic solution of Boltzmann's equation were also shown to be consistent with the values calculated from a hydrodynamic solution of Boltzmann's equation. For the cases considered, a multiterm framework was required in order to achieve accuracies to within 3% in the SST quantityprofiles.

Finally, the cross-sections calculated in [14] were used to investigate the spatio-temporal evolution of electrons in gas-phase and liquid-phase argon. The two momentum-transfer cross-sections feature different qualitative and quantitative behaviours. Striking differences in the evolution of the components of the phase-space distribution were apparent, reflecting the differences in the gas-phase and liquid-phase cross-sections, particularly the absence of a Ramsauer minimum in the liquid-phase. This highlights the problems associated with treating liquid systems as gaseous systems with increased density, which has implications for various applications including liquid argon time projection chambers. Further, it highlights the need for a complete understanding of the full space-time evolution of the electrons if

enhancements in detector accuracy are to be achieved.

Appendix A: Solution technique

The Boltzmann equation consists of two parts; an advective component (in phase space) and a component representing collisions. To solve the Boltzmann equation numerically, using a single numerical scheme for both components and a single time-stepping method, is computationally challenging Because of the complexity, we choose to replace the task of solving the full Boltzmann equation by the task of solving the configuration-space transport, and the energy-space transport with the contributions due to collisions separately, then combining the results in a manner that appropriately approximates the full solution. This can be achieved via the technique known as operator splitting [82, 83].

To this end, the Legendre polynomial expansion of Boltzmann's equation in plane parallel geometry given in equation (3) can be represented as

$$\frac{\partial f_l}{\partial t} + S_Z(f_l) + S_U(f_l) = 0, \tag{A1}$$

where

$$S_Z(f_l) = \sum_{p=\pm 1} \Delta_l^{(p)} \left(\frac{2}{m}\right)^{\frac{1}{2}} U^{\frac{1}{2}} \frac{\partial}{\partial z} f_{l+p}, \tag{A2}$$

$$S_U(f_l) = \sum_{p=\pm 1} \Delta_l^{(p)} \left(\frac{2}{m}\right)^{\frac{1}{2}} eE \left(U^{\frac{1}{2}}\frac{\partial}{\partial U} + p\frac{\left(l + \frac{3p+1}{2}\right)}{2}U^{-\frac{1}{2}}\right) f_{l+p} + J_l(f_l). \tag{A3}$$

In the following subsections we discuss numerical solution in detail, which can be here summarized as a simplified flux corrected transport method [65] for sub problem (A2), a centered difference discretization in energy and implicit Euler method in time [61] for sub problem (A2), combined via Lie-Trotter splitting [66, 67].

1. Operator splitting

The simplest method of operator splitting, and the method employed in this paper, is Lie-Trotter splitting [66, 67], which employs two separate operators, e.g. S_Z and S_U, in a sequential order. If

$$\frac{\partial f}{\partial t} + S_Z(f) + S_U(f) = 0, \tag{A4}$$

then the Lie-Trotter algorithm is

$$\frac{\partial f^*}{\partial t} + S_Z(f^*) = 0, \ \text{with} \ t \in \left[t^n, t^{n+1}\right] \ \text{and} \ f^*\left(t^n\right) = f\left(t^n\right), \tag{A5}$$

$$\frac{\partial f^\#}{\partial t} + S_U(f^\#) = 0, \ \text{ with } \ t \in \left[t^n, t^{n+1}\right] \ \text{and} \ f^\#\left(t^n\right) = f^*\left(t^{n+1}\right), \tag{A6}$$

so that $f(t^{n+1}) = f^\#\left(t^{n+1}\right)$, where t^n and t^{n+1} are successive times. This simple method can be shown to be only accurate to first order (globally) in time, and there are many other methods available that offer higher order accuracy and often include additional advantageous properties [67, 84–89]. The major reason for the choice of Lie-Trotter splitting is its computational simplicity. As described in the following sections, the numerical schemes chosen for the individual sub-problems are each (at worst) first order accurate in time, so there is little to be gained by using a higher order and more computationally expensive operator splitting method [83]. A secondary reason is that, if S_Z is treated in an explicit manner and S_U is treated in an implicit manner, then the overall result is essentially the Douglas class of the Alternating Direction Implicit schemes [90, 91], which is particularly successful at accurately capturing the steady-state solution. We compare the asymptotic values from the current non-hydrodynamic formalism with the results of hydrodynamic calculations for a benchmark model in Section III A. Although general operator-splitting schemes can capture the relaxation process, accurately and consistently determining the steady-state solution can be very difficult [92].

The isolation of the configuration-space dependence to the operator S_Z makes this particular scheme an example of dimensional splitting. We can now investigate how we treat the configuration-space advection and energy-space advection and collision components numerically in detail.

2. Configuration-space advection

The operator involving the configuration-space dependence, S_z, is given by equation (A2), which represents a coupled homogeneous advection equation. As there are no derivatives of U present in S_z, the configuration-space dependence can be solved independently for different values of U which is huge simplification when a discretization in energy space is used. The coupled advection equation can be simplified as follows:

$$\frac{\partial}{\partial t} f_l + \left(\frac{2U}{m}\right)^{\frac{1}{2}} \Delta_l^{(-)} \frac{\partial}{\partial z} f_{l-1} + \left(\frac{2U}{m}\right)^{\frac{1}{2}} \Delta_l^{(+)} \frac{\partial}{\partial z} f_{l+1} = 0, \tag{A7}$$

which can be written in matrix form,

$$\frac{\partial}{\partial t}\mathbf{f} + \mathbf{A}\frac{\partial}{\partial z}\mathbf{f} = \mathbf{0}, \tag{A8}$$

where $\mathbf{f} = [f_0, f_1, ..., f_{l_{\max}}]^\mathrm{T}$ and

$$\mathbf{A} = \left(\frac{2U}{m}\right)^{\frac{1}{2}} \begin{bmatrix} 0 & \Delta_0^{(+)} & & & \\ \Delta_1^{(-)} & 0 & \Delta_1^{(+)} & & \\ & \ddots & \ddots & \ddots & \\ & & \Delta_{l_{\max}-1}^{(-)} & 0 & \Delta_{l_{\max}-1}^{(+)} \\ & & & \Delta_{l_{\max}}^{(-)} & 0 \end{bmatrix}. \tag{A9}$$

By letting $\mathbf{A} = \mathbf{R\Lambda R^{-1}}$, where $\mathbf{\Lambda}$ is a matrix of eigenvalues of $\mathbf{A}$ on the diagonal, and $\mathbf{R}$ are the associated eigenvectors, then

$$\frac{\partial}{\partial t}\mathbf{g} + \mathbf{\Lambda}\frac{\partial}{\partial z}\mathbf{g} = \mathbf{0}, \tag{A10}$$

where $\mathbf{g} = \mathbf{R^{-1}f}$, which now represents a set of uncoupled, homogeneous advection equations. It follows from the method of characteristics [93], that

$$\mathbf{g}\left(t, z\right) = \mathbf{g}\left(0, z - \mathbf{\Lambda}t\right). \tag{A11}$$

Even in this extremely simple form, the solution can be troublesome. When discretized, the set of values $z - \mathbf{\Lambda}t$ are unlikely to align with existing z values, and hence some form of interpolation is required. It can be shown that linear interpolation is equivalent to a first order upwind finite volume method scheme [94]. First order methods have the advantage of being well behaved and can be used to conserve mass etc. with no unwanted, unphysical

27

oscillations, but have the disadvantage of introducing extra numerical diffusion, particularly around regions of sharp variation [95]. Higher order methods perform better at controlling unwanted diffusion but can lead to problematic, oscillatory and unphysical solutions. Rather than straightforward interpolation, we choose to employ a variation of a technique well known in fluid transport, the SHASTA algorithm of Boris and Book [65]. The SHASTA algorithm approach, termed flux-corrected transport (FCT), leads to a class of Eulerian finite-difference algorithms which strictly enforce the non-negative property of realistic mass and energy densities. As a result, steep gradients and shocks can be handled particularly well, which is a useful property when modelling transport under non-hydrodynamic conditions. A FCT algorithm consists conceptually of two major stages, a transport or convective stage, followed by an anti-diffusive or corrective stage.

We employ a simplified version of the full FCT algorithm to numerically approximate $\mathbf{g}\left(0, z - \mathbf{\Lambda}t\right)$. Let us consider the evolution of $\mathbf{g}\left(t, z\right)$ for a single $\mathbf{\Lambda}$, i.e., $g\left(t, z; \Lambda\right)$, over a time interval of Δt, with a uniform configuration-space mesh with spacing Δz. By discretizing in this way, $z_j = j\Delta z$ for $j = 1, 2 \ldots, n_z - 1$, and $t_{n+1} = t_n + \Delta t$. The algorithm is as follows:

1. **Shift:** The elements of $g\left(t, z; \Lambda\right)$ are shifted to the node closest to $z - \beta$, where $\beta = \frac{\Delta t}{\Delta z}\Lambda$. This may result in an 'overshoot', but we can then propagate the shifted solution (in step 2) either forwards or backwards in time as appropriate. The purpose of this step is to overcome time step limitations due to the Courant-Friedrichs-Levy (CFL) condition [96], which allows us to choose arbitrary time step sizes with respect to the configuration-space convergence (sufficiently small time steps are still necessary for the operator splitting accuracy etc.). By shifting to the nearest node, the CFL condition

$$|\beta| = \frac{\Delta t}{\Delta z}|\Lambda| \leq 1 \tag{A12}$$

   for the remaining advection is always satisfied.

2. **Advection with additional diffusion:** The advection algorithm employed is given by

$$g_j^{n+1} = g_j^n - \frac{\beta'}{2}\left(g_{j+1}^n - g_{j-1}^n\right) + \left(\gamma + \frac{\beta'^2}{2}\right)\left(g_{j+1}^n - 2g_j^n + g_{j-1}^n\right), \tag{A13}$$

   where $g_j^{n+1} = g\left(t_{n+1}, z_j\right)$, and

$$\gamma = \left[0, \frac{\beta'}{2}\right], \tag{A14}$$

28

is the additional numerical diffusion. The dimensionless advancement $\beta' = \beta - \lfloor\beta\rfloor$ accounts for the shift that has been applied in step 1. Note that β' may be opposite in sign to β, which corresponds to an overshoot in step 1. However, this does not adversely affect the procedure. If $\gamma = 0$, then equation (A13) is the well known Lax-Wendroff scheme [95], which is accurate to second order. Historically, the inclusion of an extra diffusion term, γ, has been used to ensure that a density function (i.e. a function that is non-negative by definition) remains positive, which is unconditionally enforced everywhere if $\gamma = \frac{\beta'}{2}$. In our case, the g_j^n include contributions from $f_{l\geq 1}$, which are expected to be negative in some regions of space. However, the presence of γ ensures the stability of g_j^{n+1}, which can be defined by the requirement that $\Delta g_j^{n+1} < \max(\Delta g_{j-1}^n, \Delta g_j^n, \Delta g_{j+1}^n)$ where $\Delta g_j^n = g_{j+1}^n - g_j^n$. When the solution g_j^n is sharply varying or, in the extreme case, a discontinuity, the additional diffusion is necessary to suppress unphysical oscillatory behaviour in g_j^{n+1}.

3. **Anti-diffusion:** An 'anti-diffusion' step is employed to reduce the extra numerical diffusion introduced in (A13) i.e.,

$$\bar{g}_j^{n+1} = g_j^{n+1} - \left(\gamma + \frac{\beta^2}{2}\right)\left(g_{j+1}^{n+1} - 2g_j^{n+1} + g_{j-1}^{n+1}\right). \tag{A15}$$

The inclusion of this extra diffusion in step 2 assures that the solution is positive and physically realistic, and the straightforward application of step 3 undoes this which can re-introduce a negative solution. Boris and Book [65] suggested modifying the removal of the erroneous diffusion by just enough to maintain positivity, in a non-linear way (note that they worked with non-negative densities, as we have remarked on above in step 2). This is an early example and precursor of the modern technique of flux limiting [97–101]. In this work the full anti-diffusion step is applied in general, except in regions where a sharp variation or discontinuity is known *a priori* (e.g. configuration-space boundaries), in which case no anti-diffusion is applied. Unphysical oscillations can now occur, but we have found that for the situations considered they are negligibly small. The natural extension is to include flux limiting to prevent this unphysical behavior but this introduces extra computational complexity.

It should be noted that the shift step can be performed after the advection and anti-diffusion stages with no change in the result. We have assumed that the boundaries are absorbing,

29

in that the elements of $g(t, z)$ that move outside the computational domain are lost, and no information is introduced from outside the domain. Although perfectly absorbing boundaries are notoriously difficult to implement numerically, in our calculations we avoid this problem by keeping the swarm density negligible at the simulation edges, through the use of an adaptive mesh, see Section A 4. In practice we pre-calculate a transformation matrix (for a given set of parameters) which combines the above three steps for each of the grid energies.

3. Energy-space advection and collisions

A major advantage of splitting the Boltzmann equation operator according to equations (A2)-(A3) is that S_U is then the familiar, spatially homogeneous Boltzmann equation. There is much literature on solving this equation, and we use the approach developed previously [14, 61, 102, 103] to perform the numerical discretization and time-step. A full description of the numerical solution of the process is given in [61], and we will briefly summarize it here. The equation we need to solve is equation (A3). The time dimension is discretized with a first order implicit Euler method, which has been chosen for its good stability properties. Similar to the work of Winkler and collaborators [104–106], we employ a finite difference method to discretize the system of ODE's at centred points using a centred difference scheme, i.e.,

$$\left.\frac{df(U,t)}{dU}\right|_{U_{i+1/2}} = \frac{f(U_{i+1}, t) - f(U_i, t)}{U_{i+1} - U_i}, \tag{A16}$$

$$f(U_{i+1/2}, t) = \frac{f(U_{i+1}, t) + f(U_i, t)}{2}, \tag{A17}$$

so that equation (A3) evaluated at $i + 1/2$ becomes,

$$S_U\left(f_l\right)|_{i+1/2} = J_l\left(f_l\right)|_{i+1/2} + \left(\frac{2}{m}\right)^{\frac{1}{2}} \sum_{p=\pm 1} \Delta_l^{(p)} eE\left[U_{i+1/2}^{\frac{1}{2}}\left(\frac{f_{l+p}(U_{i+1}, t) - f_{l+p}(U_i, t)}{U_{i+1} - U_i}\right)\right.$$
$$\left. + p\frac{\left(l + \frac{3p+1}{2}\right)}{2}U_{i+1/2}^{-\frac{1}{2}}\left(\frac{f_{l+p}(U_{i+1}, t) + f_{l+p}(U_i, t)}{2}\right)\right]. \tag{A18}$$

Although a general form can be constructed for an arbitrary grid, the simplest case is for evenly spaced points, i.e.

$$U_i = i\Delta U \quad \text{for} \quad 0 \le i \le n_U, \tag{A19}$$

where ΔU is a constant. By discretizing at the midpoint of the two solution nodes results in a system of linear equations that is under-determined. The extra information is naturally provided by boundary conditions which are appended to the system.

These boundary conditions have been analyzed by Winkler and collaborators [104–106] who investigated the multi-term, even order approximation, and discovered that the general solution of the steady-state hierarchy contains $\frac{1}{2}(l_{\max} + 1)$ non-singular and $\frac{1}{2}(l_{\max} + 1)$ singular fundamental solutions when U approaches infinity, and the physically relevant solution has to be sought within the non-singular set of fundamental solutions. The boundary conditions necessary for the determination of the non-singular physically relevant solution are [104]

$$f_l(U = 0) = 0 \ \text{ for odd } l,$$

$$f_l(U = U_\infty) = 0 \ \text{ for even } l, \tag{A20}$$

$$f_l(U > U_\infty) = 0 \ \text{ for all } l,$$

where U_∞ represents a sufficiently large energy. In practice, U_∞ has to be determined in a prior calculation, and is chosen such that the value of $f_0(U_\infty)$ is less than 10^{-10} of the maximum value of f_0.

The temporal evolution of the system of coupled linear equations

$$\frac{\partial f_l}{\partial t} = -S_U(f_l),$$

is achieved using a first-order implicit Euler method, which has been chosen for its good stability properties. The first-order implicit Euler method leads to a system of the form

$$\left[\frac{1}{t_{n+1} - t_n} + S_U \right] f_l(U, t_{n+1}) = \frac{f_l(U, t_n)}{t_{n+1} - t_n}. \tag{A21}$$

4.   Numerical considerations and adaptive meshing

The matrix system of linear equations that result from the discretization of the Legendre-decomposed Boltzmann equation in energy- and configuration-space at each time step are of the size $(n_z n_U (l_{\max} + 1)) \times (n_z n_U (l_{\max} + 1))$, where n_z and n_U are the number of nodes in configuration and energy space respectively. Due to the discretization schemes, the matrix

31

is sparse and sparse techniques are employed in the code to exploit this property. Each of these parameters are free to be increased until some convergence criterion is met. It should be noted that, although the two-term approximation ($l_{\max} = 1$) has been used extensively, it is well known that it can be insufficient in many situations [49].

In order to model the spatio-temporal relaxation of a narrow Gaussian source distribution in configuration-space with a distribution of energies as computationally efficiently as possible, we have developed a configuration-space node-mesh that adaptively follows the spread of the distribution throughout the simulation. In this way, a small configuration-space window is used around the original narrow Gaussian source which can then be sufficiently resolved with a small n_z. As the initial pulse drifts and diffuses, a small amount of information reaches and then leaks out of the window boundaries. Before the amount of information lost to the system exceeds some small tolerance, the window is extended and the solution at the previous time-step is calculated on the new configuration-space mesh. This approach differs from existing adaptive mesh procedures developed for direct kinetic solvers, which utilize 'tree of tree' data structures [51, 52].We have found that the most convenient way to quantify the amount of information on the boundary is by the relative number density, and impose the condition that when

$$\int_{t_0}^{t} dt' \ \frac{n\left(z_{\mathrm{L}} \text{ or } z_{\mathrm{R}}, t'\right)}{\int dz \ n(z, t')} \geq 10^{-5}, \tag{A22}$$

then the configuration-space window is doubled (while the number of nodes is kept the same). Here t_0 is the time of the last window adjustment, z_{L} and z_{R} are locations of the left and right configuration-space boundaries respectively. The decision to extend the window by doubling has been made so that the new mesh lines up exactly with nodes of the old mesh, hence requiring no interpolation. The accuracy of the modified Lax-Wendroff scheme used to model the configuration-space advection [95] is related to the parameter $\beta = \frac{\Delta t}{\Delta z}\Lambda$, hence by doubling Δz after a re-adjustment, the value of Δt can also be doubled. This effectively allows us to use smaller time steps when our solution is sharp and diffusing quickly, and larger time steps once the solution has spread out and is varying less quickly. A maximum value for the time step size still needs to be enforced however, since with bigger time step sizes less mixing between the configuration-space and energy-space components of the operator splitting occurs, leading to errors.

If the spatial discretization is of similar size to features in the spatial profiles, such as a

Franck-Hertz oscillation wavelength, then it will be very difficult to accurately resolve these features in the distributions and consequently the time-averaged profiles. Of course, the initial choice for the discretization is small enough to easily resolve the important features, but as the simulation progresses and the distribution diffuses, the adaptive mesh will increase in range and also increase the spatial discretization step size. The distribution is also drifting in space to larger z, which means that contributions to the time-averaged quantities from solutions with larger spatial discretizations are significant only for z past a particular point. If we let λ be the Franck-Hertz wavelength, then there will be a time in the simulation t_λ after which the spatial discretization becomes $\Delta z > \lambda/10$, and we can expect that the oscillations are not accurately represented. We define a point z_λ, such that there is a negligible contribution to the time-averaged quantity for $z < z_\lambda$ from the Green's function solution for $t > t_\lambda$. In this paper, we choose z_λ as the point beyond which more than 99% of the number density profile has propagated at the time t_λ. After this point, the coarseness of the discretization causes the distribution to slowly lose its features, which manifests itself in the time-averaged quantities by the suppression of the amplitude and a phase-lag of the oscillations. Hence, we should expect that the results for $z > z_\lambda$ to progressively deviate from the true spatially dependent steady-state values, until the oscillations are completely dampened. It is clear that increasing the resolution in configuration-space will mitigate this problem, but is also more computationally intensive.

There is one extra complication to be discussed. Since the boundaries are absorbing, when they are re-adjusted, the number density profiles (and distribution functions) drop directly from the built-up value at the previous boundaries location to zero in a single Δz, which can lead to problematic, unphysical, oscillatory solutions when treated with the method described in Section A 2. In order to combat this, we simply apply the procedure described in Section A 2 without the final anti-diffusion step for a small amount of time on the edge and in the newly opened regions. The extra diffusion added ensures that the solution remains positive and gives physical results, which, after a small amount of time, ensures that the profiles decrease smoothly to zero at the boundary. After this short correction time, we again apply the full procedure. By not removing the added extra diffusion we have increased the overall diffusion, but since it is only applied for a small time and to a region where there is necessarily only a small proportion of particles, this does not significantly affect the transport

profiles.

[1] W. Schmidt, *Liquid state electronics of insulating liquids* (CRC Press, Boca Raton, 1997).

[2] A. Marchionni, Annual Review of Nuclear and Particle Science **63**, 269 (2013).

[3] E. Aprile, K. Arisaka, F. Arneodo, A. Askin, L. Baudis, A. Behrens, K. Bokeloh, E. Brown, J. M. R. Cardoso, B. Choi, et al. (XENON100 Collaboration), Physical Review Letters **105**, 131302 (2010).

[4] E. Aprile, J. Angle, F. Arneodo, L. Baudis, A. Bernstein, A. Bolozdynya, P. Brusov, L. C. C. Coelho, C. E. Dahl, L. DeViveiros, et al., Astroparticle Physics **34**, 679 (2011), 1001.2834.

[5] T. Sumner, New Astronomy Reviews **49**, 277 (2005).

[6] M. G. Kong, G. Kroesen, G. Morfill, T. Nosenko, T. Shimizu, J. van Dijk, and J. L. Zimmermann, New J. Phys. **11**, 115012 (2009).

[7] W. Tian and M. J. Kushner, J. Phys. D **47**, 165201 (2014).

[8] S. A. Norberg, W. Tian, E. Johnsen, and M. J. Kushner, J. Phys. D **47**, 475203 (2014).

[9] C. Chen, D. X. Liu, Z. C. Liu, A. J. Yang, H. L. Chen, G. Shama, and M. G. Kong, **34**, 403 (2014).

[10] Y. Zheng, J. R. Wagner, and L. Sanche, Phys. Rev. Lett. **96**, 208101 (2006).

[11] A. M. Munoz, C. Fuss, M. A. Cortes-Giraldo, S. Incerti, V. Ivanchenko, A. Ivanchenko, J. M. Quesada, F. Salvat, C. Champion, and G. Garcia, *Monte Carlo Methods to Model Radiation Interactions and Induced Damage* (Springer, New York, 2012).

[12] R. White, J. Sullivan, A. Bankovic, S. Dujko, R. Robson, Z. L. Petrovic, G. Garcia, M. Brunger, and S. Buckman, *Positron and Electron Interactions and Transport in Biological Media: Modeling Tracks and Radiation Damage* (Springer, New York, 2012).

[13] H. Nikjoo, D. Emfietzoglou, R. Watanabe, and S. Uehara, Radiation Physics and Chemistry **77**, 1270 (2008).

[14] G. J. Boyle, R. P. McEachran, D. G. Cocks, and R. D. White, J. Chem. Phys. **142**, 154507 (2015).

[15] J. Lekner, Phys. Rev. **158**, 130 (1967).

[16] M. H. Cohen and J. Lekner, Phys. Rev. **158**, 305 (1967).

[17] R. E. Robson and K. F. Ness, Phys. Rev. A **33**, 2068 (1986).

[18] R. D. White, K. F. Ness, R. E. Robson, and B. Li, Phys. Rev. E **60**, 2231 (1999).

[19] R. D. White, K. F. Ness, and R. E. Robson, Applied Surface Science **192**, 26 (2002).

[20] R. D. White, R. E. Robson, S. Dujko, P. Nicoletopoulos, and B. Li, J. Phys. D: Appl. Phys. **42**, 194001 (2009).

[21] D. Loffhagen and F. Sigeneger, Plasma Sources Sci. Technol. **18**, 034006 (2009).

[22] B. Li, R. D. White, and R. E. Robson, J. Phys. D: Appl. Phys. **35**, 1 (2002).

[23] I. A. Porokhova, Y. B. Golubovskii, J. Bretagne, M. Tichy, and J. F. Behnke, Phys. Rev. E **71**, 066406 (2005).

[24] I. A. Porokhova, Y. B. Golubovskii, J. Bretagne, M. Tichy, and J. F. Behnke, Phys. Rev. E **71**, 066407 (2005).

[25] J. Frank and G. Hertz, Verh. Deutsche Phys. Ges. **16**, 457 (1914).

[26] R. E. Robson, B. Li, and R. D. White, J. Phys. B: At. Mol. Opt. Phys. **33**, 507 (2000).

[27] R. Winkler and F. Sigeneger, J. Phys. D: Appl. Phys. **34**, 3407 (2001).

[28] R. Winkler, F. Sigeneger, and D. Uhrlandt, Pure Appl. Chem. **68**, 1065 (1996).

[29] F. Sigeneger and R. Winkler, Plasma Chemistry and Plasma Processing **17**, 1 (1997).

[30] F. Sigeneger and R. Winkler, Plasma Chemistry and Plasma Processing **17**, 281 (1997).

[31] R. Winkler, G. Petrov, F. Sigeneger, and D. Uhrlandt, Plasma Sources Sci. Technol. **6**, 118 (1997).

[32] D. Loffhagen, F. Sigeneger, and R. Winkler, Plasma Process. **18**, 153 (2003).

[33] F. Sigeneger, Y. B. Golubovskii, I. A. Porokhova, and R. Winkler, Plasma Chem. and Plasma Process. **20**, 429 (1998).

[34] F. Sigeneger and R. Winkler, Plasma Chem. and Plasma Process. **20**, 429 (2000).

[35] F. Sigeneger, G. I. Sukhinin, and R. Winkler, Plasma Chem. and Plasma Process. **20**, 87 (2000).

[36] Y. B. Golubovskii, R. V. Kozakov, V. A. Maiorov, J. Behnke, and J. F. Behnke, Phys. Rev. E **62**, 2707 (2000).

[37] Y. B. Golubovskii, A. Y. Skoblo, V. A. Maiorov, and V. O. Nekutchaev, Plasma Sources Sci. Technol. **11**, 309 (2002).

[38] Y. B. Golubovskii, I. A. Porokhova, J. Behnke, and V. O. Nekutchaev, J. Phys. D: Appl. Phys. **31**, 2447 (1998).

[39] Y. B. Golubovskii, V. A. Maiorov, I. A. Porokhova, and J. Behnke, J. Phys. D: Appl. Phys.

32, 1391 (1999).

[40] B. Li, R. E. Robson, and R. D. White, Phys. Rev. E **74**, 026405 (2006).

[41] S. Dujko, R. D. White, Z. L. Petrović, R. E. Robson, and Z. L. Petrovi, Plasma Sources Science and Technology **20**, 024013 (2011).

[42] K. Rupp, C. Jungemann, S. M. Hong, M. Bina, T. Grasser, and A. JÃŒngel, Journal of Computational Electronics **15**, 939 (2016).

[43] W. J. Goedheer and P. M. Meijer, J. Nucl. Mater. **200**, 282 (1993).

[44] M. O. M. Mahmoud and M. Yousfi, J. Appl. Phys. **81**, 5935 (1997).

[45] D. Loffhagen and R. Winkler, J. Phys. D: Appl. Phys. **34**, 1355 (2001).

[46] V. I. Kolobov, Computational Materials Science **28**, 302 (2003).

[47] A. R. Bell, A. P. L. Robinson, M. Sherlock, R. J. Kingham, and W. Rozmus, Plasma Physics and Controlled Fusion **48**, R37 (2006).

[48] V. I. Kolobov and R. R. Arslanbekov, IEEE Transactions on Plasma Science **34**, 895 (2006).

[49] R. D. White, R. E. Robson, B. Schmidt, and M. Morrison, Journal of Physics D: Applied Physics **36**, 3125 (2003).

[50] V. I. Kolobov, Physics of Plasmas **20**, 101610 (2013).

[51] R. R. Arslanbekov, V. I. Kolobov, and A. A. Frolova, Physical Review E **88**, 063301 (2013).

[52] V. I. Kolobov and R. R. Arslanbekov, Journal of Computational Physics **231**, 839 (2012).

[53] P. Segur, A. Alkaa, S. Pineau, A. Zahraoui, B. Chouki, C. Moutarde, and S. Laffont, *(null)* (1995).

[54] P. Segur, M. Yousfi, and M. C. Bordage, Journal of Physics D: Applied Physics **17**, 2199 (1984).

[55] K. Maeda and T. Makabe, Japanese Journal of Applied Physics **33**, 4173 (1994).

[56] H. Sugawara, Y. Sakai, and H. Tagashira, Journal of Physics D: Applied Physics **25**, 1483 (1992).

[57] M. Shoucri, *Physics Research and Technology : Eulerian Codes for the Numerical Solution of the Kinetic Equations of Plasmas* (Nova Science Pub Inc, Hauppauge, New York, 2010).

[58] S. Dujko, R. D. White, and Z. L. Petrovic, J. Phys. D: Appl. Phys. **41**, 245205 (2008).

[59] Z. L. Petrović, S. Marjanović, S. Dujko, A. Banković, G. Malović, S. Buckman, G. Garcia, R. White, and M. Brunger, Applied radiation and isotopes **83**, 148 (2013).

[60] S. Dujko, Z. M. Raspopović, R. D. White, T. Makabe, and Z. L. Petrović, The European

Physical Journal D **68**, 166 (2014).

[61] G. J. Boyle, W. J. Tattersall, D. G. Cocks, S. Dujko, and R. D. White, Phys. Rev. A **91**, 052710 (2015).

[62] R. D. White and R. E. Robson, Phys. Rev. E **84**, 031125 (2011).

[63] R. D. White, R. E. Robson, B. Schmidt, and M. A. Morrison, J. Phys. D: Appl. Phys. **36**, 3125 (2002).

[64] R. White and R. Robson, Phys. Rev. Lett. **102**, 230602 (2009).

[65] J. P. Boris and D. L. Book, J. Comp. Phys. **11**, 38 (1973).

[66] K. A. Bagrinovskii and S. K. Godunov, Dokl. Akad. Nauk SSSR (NS) **115**, 431 (1957).

[67] G. Strang, SIAM J. Numer. Anal. **5**, 506 (1968).

[68] L. Huxley and R. Crompton, *The Diffusion and Drift of Electrons in Gases* (Wiley, New York, 1974).

[69] S. Dujko, Z. M. Raspopovic, and Z. L. Petrovic, J. Phys. D: Appl. Phys. **38**, 2952 (2005).

[70] W. J. Tattersall, D. G. Cocks, G. J. Boyle, S. J. Buckman, and R. D. White, Phys. Rev. E **91**, 043304 (2015).

[71] M. Wertheim, Phys. Rev. Lett. **10**, 321 (1963).

[72] E. Thiele, J. Chem. Phys. **39**, 474 (1963).

[73] L. Verlet and J. Weis, Phys. Rev. A **5**, 939 (1971).

[74] W. Megen and P. Pusey, Phys. Rev. A **43**, 5429 (1991).

[75] G. J. Boyle, R. D. White, R. E. Robson, S. Dujko, and Z. L. Petrovic, New J. Phys. **14**, 045011 (2012).

[76] B. Li, Ph.D. thesis, James Cook University (1999).

[77] J. Fletcher, J. Phys. D: Appl. Phys. **18**, 221 (1985).

[78] P. Segur, A. Alkaa, S. Pineau, Z. A, A. Chouki, C. Moutarde, and S. Laffront, Plasma Sources Sci. Technol. **4**, 183 (1995).

[79] G. Petrov and R. Winkler, J. Phys. D: Appl. Phys. **30**, 53 (1997).

[80] R. D. White, R. E. Robson, P. Nicoletopoulos, and S. Dujko, The European Physical Journal D **66**, 117 (2012).

[81] M. Foxe, C. Hagmann, I. Jovanovic, A. Bernstein, K. Kazkaz, V. Mozin, S. V. Pereverzev, S. Sangiorgio, and P. Sorensen, Nucl. Instr. Meth. Phys. Res. A **771**, 88 (2015).

[82] J. G. Verwer and B. Sportisse, Technical Report MAS-R9830 **CWI** (1998).

[83] I. Farago and A. Havasiy, *Operator Splittings and their Applications* (Nova Science Publishers Inc., New York, 2009).

[84] B. O. Dia and M. Schatzman, Math. Mod. Numer. Anal. **30**, 343 (1996).

[85] T. Ohwada, J. Comp. Phys. **139**, 1 (1998).

[86] A. Gerisch and R. Weiner, Comp. Math. App. **45**, 53 (2003).

[87] L. Pareschi and G. Russo, Adv. Theor. Comp. Math. **3**, 269 (2000).

[88] L. Pareschi and G. Russo, SIAM. J. Numer. An. **37**, 1217 (2005).

[89] S. Gottlieb and C.-W. Shu, Math. Comp. **67**, 73 (1998).

[90] J. Douglas, Numer. Math. **4**, 41 (1962).

[91] J. Douglas and J. E. Gunn, Numer. Math. **6**, 428 (1964).

[92] W. Hundsdorfer, Applied Numerical Mathematics **42**, 213 (2002).

[93] A. D. Polyanin, *Handbook of Linear Partial Differential Equations for Engineers and Scientists.* (Chapman and Hall, Boca Raton, 2002).

[94] M. Morales-Hernandez, P. Garcia-Navarro, and J. Murillo, J. Comp. Phys. **231**, 6532 (2012).

[95] R. LeVeque, *Finite Difference Methods for Ordinary and Partial Differential Equations* (SIAM, Philadelphia, 2007).

[96] R. Courant, K. Friedrichs, and H. Lewy, IBM J. Res. Dev. **11**, 215 (1967).

[97] A. Harten, J. Comp. Phys. **49**, 357 (1983).

[98] S. Osher and S. Chakravarthy, SIAM J. Numer. Anal. **21**, 995 (1984).

[99] P. L. Roe, Royal Aircraft Establishment Technical Report 81047 (1981).

[100] S. T. Zalesak, J. Comp. Phys. **31**, 335 (1979).

[101] P. K. Sweby, SIAM J. Nume. Anal. **21**, 995 (1984).

[102] G. J. Boyle, M. J. E. Casey, R. D. White, Y. Cheng, and J. Mitroy, J. Phys. D: Appl. Phys. **47**, 345203 (2014).

[103] G. J. Boyle, M. J. E. Casey, R. D. White, and J. Mitroy, Phys. Rev. A **89**, 022712 (2014).

[104] R. Winkler, G. L. Braglia, A. Hess, and J. Wilhelm, Beitr. Plasmaphys. **24**, 657 (1984).

[105] D. Loffhagen and R. Winkler, J. Phys. D: Appl. Phys. **29**, 618 (1996).

[106] H. Leyh, D. Loffhagen, and R. Winkler, Comp. Phys. Comm. **113**, 33 (1998).